



## Engineering dual-exsolution on self-assembled cathode to achieve efficient electrocatalytic CO<sub>2</sub> reduction

Feng Hu<sup>a</sup>, Yihan Ling<sup>b</sup>, Siyu Fang<sup>a</sup>, Longtao Sui<sup>a</sup>, Huangwei Xiao<sup>a</sup>, Yonglong Huang<sup>a</sup>, Sijiao Wang<sup>a</sup>, Beibei He<sup>a,c,d,\*</sup>, Ling Zhao<sup>a,c,d,\*</sup>

<sup>a</sup> Faculty of Materials Science and Chemistry, China University of Geosciences, Wuhan 430074, China

<sup>b</sup> School of Materials Science and Physics, China University of Mining and Technology, Xuzhou 221116, China

<sup>c</sup> Zhejiang Institute, China University of Geosciences (Wuhan), Hangzhou 311305, China

<sup>d</sup> Shenzhen Research Institute, China University of Geosciences, Shenzhen 518000, China



### ARTICLE INFO

#### Keywords:

Dual-exsolution  
Self-assembly  
Cathode materials  
Solid oxide electrolysis cells  
CO<sub>2</sub> reduction reaction

### ABSTRACT

Solid oxide electrolysis cells (SOEC) hold great promise for efficiently converting CO<sub>2</sub> into valuable products. However, their commercial viability is impeded by the sluggish kinetics of CO<sub>2</sub> reduction reaction (CO<sub>2</sub>RR). Herein, we propose a novel approach of dual-exsolution on self-assembled cathode for SOEC to achieve efficient CO<sub>2</sub>RR. Induced by in-situ exsolution, metallic Ni nanoparticles are created on both Ni doped Sr<sub>2</sub>Fe<sub>1.5</sub>Mo<sub>0.5</sub>O<sub>6-δ</sub> (Ni-SFM) and Ni doped Gd<sub>0.1</sub>Ce<sub>0.9</sub>O<sub>2-δ</sub> (Ni-GDC) surfaces. As a demonstration, a SOEC with the Ni@Ni-SFM/Ni-GDC cathode delivers a high current density of 1.72 A cm<sup>-2</sup> at 800 °C and 1.5 V and exhibits favorable durability for 100 h, rivaling most of the state-of-the-art cathode materials of SOEC for CO<sub>2</sub>RR. Theoretical calculations reveal that not only exsolved Ni@Ni-SFM heterointerface but also exsolved Ni@Ni-GDC heterointerface are intrinsically active for CO<sub>2</sub>RR. This protocol offers new insights into designing dual-exsolved self-assembled cathode materials for high-temperature CO<sub>2</sub> electrolysis.

### 1. Introduction

To combat global climate change and energy crisis, green and low-carbon development has become an international consensus. Electrocatalytic CO<sub>2</sub> reduction reaction (CO<sub>2</sub>RR) into value-added fuels or chemicals is increasingly attractive as an advanced strategy to achieve carbon neutral, especially when powered via renewable solar, wind, and tide energies [1–3]. Nevertheless, the CO<sub>2</sub>RR is facing with the challenges of sluggish kinetics and unmanageable product selectivity because of the thermodynamically stable CO<sub>2</sub> molecule and the complex competing electrochemical processes, particularly at low temperatures and in solution systems [4–7]. Benefiting from high energy efficiency and excellent selectivity, the CO<sub>2</sub>RR performed by intermediate temperature solid oxide electrolysis cells (SOEC) technology has been emerging in recent years [8–14].

Traditional Ni-based cermets are widely utilized as available cathodes of SOEC for water electrolysis owing to their exceptional electrical conductivity and high electrocatalytic activity. Unfortunately, the practical application of Ni-based cathodes for CO<sub>2</sub>RR usually encounter

bottlenecks of carbon deposition and redox instability [15–18]. On the contrary, endowed with variable composition, tunable electronic structure, and excellent redox stability, mixed electronic-ionic conducting perovskite oxides, including Sr<sub>2</sub>Fe<sub>1.5</sub>Mo<sub>0.5</sub>O<sub>6-δ</sub> (SFM) [19–21], (La,Sr)Cr<sub>0.5</sub>Mn<sub>0.5</sub>O<sub>3-δ</sub> (LSCM) [22], (La,Sr)FeO<sub>3-δ</sub> (LSF) [23,24], and (La, Sr)TiO<sub>3+δ</sub> (LST) series [25], have been extensively investigated as alternative cathode materials to drive CO<sub>2</sub>RR. Nevertheless, their electrocatalytic activity are still far away from desirable, typically inferior to those of Ni-based cermets.

Boosting the electrocatalytic performance of perovskite oxides can be achieved through various strategies, such as component designing [10,26–28], infiltration tailoring [29–31], and in-situ exsolution engineering [32–41] et al. Of these, in-situ exsolution of metal nanoparticles on perovskite surface ensures several merits: (1) highly active metal nanoparticles and oxygen vacancies-rich perovskite are simultaneously created, (2) metal-oxide heterointerfaces potentially induce synergistic effect for catalyzing CO<sub>2</sub>RR, (3) well-anchored structure efficiently inhibits carbon deposition and metal nanoparticle aggregation, (4) exsolution/dissolution processes are reversible during redox cycles for

\* Corresponding authors at: Faculty of Materials Science and Chemistry, China University of Geosciences, Wuhan 430074, China.

E-mail addresses: [hebb@cug.edu.cn](mailto:hebb@cug.edu.cn) (B. He), [zhaoling@cug.edu.cn](mailto:zhaoling@cug.edu.cn) (L. Zhao).

practical application. For example, the exsolution of RuFe alloy nanoparticles on  $\text{Sr}_2\text{Fe}_{1.4}\text{Ru}_{0.1}\text{Mo}_{0.5}\text{O}_{6-\delta}$  perovskite with the facilitated  $\text{CO}_2$  adsorption capacity delivered a remarkably enhanced  $\text{CO}_2\text{RR}$  activity [40]. Similarly, core-shell structured NiFe/FeO<sub>x</sub> exsolved on  $\text{Pr}_{0.4}\text{Sr}_{1.6}\text{Ni}_{0.2}\text{Fe}_{1.3}\text{Mo}_{0.5}\text{O}_{6-\delta}$  perovskite enabled rich metal-oxide interfaces that were electrochemically active for  $\text{CO}_2$  adsorption and activation [41]. On the other hand, transition metals exsolved on doped cerium oxides also demonstrated low  $\text{CO}_2$  dissociation and CO desorption barriers, contributing to outstanding  $\text{CO}_2\text{RR}$  activity [42].

Besides intrinsic electrocatalytic activity, perovskite oxides cooperated with oxygen ionic conductors, e.g. doped cerium oxides, can not only increase oxygen ionic transport capacity in cathodes to enlarge three phase boundaries but also play as potential electrocatalysts for  $\text{CO}_2\text{RR}$ . Prepared by mechanical grinding or infiltration methods, composite cathodes consisting of perovskite and doped ceria demonstrate higher  $\text{CO}_2\text{RR}$  performance than pristine perovskites [19,43,44]. However, these methods usually suffer from a cumbersome preparation process and hardly achieve uniformly distribution. Recently, a self-assembly strategy has been proposed for facile synthesis of composite electrodes with strong interactions, plentiful heterointerfaces, congenital chemical and thermal compatibility [45–50]. One critical challenge is how to intelligently tailor self-assembled cathodes with the desirable components and microstructures.

Motivated via the concepts of exsolution and self-assembly, we, for the first time, develop a novel dual-exsolved self-assembled cathode of SOEC for  $\text{CO}_2\text{RR}$ . Conducted by an elegant one-pot synthesis, the composite cathode is self-assembled into two phases of Ni doped  $\text{Sr}_2\text{Fe}_{1.5}\text{Mo}_{0.5}\text{O}_{6-\delta}$  (Ni-SFM) and Ni doped  $\text{Gd}_{0.1}\text{Ce}_{0.9}\text{O}_{2-\delta}$  (Ni-GDC). Interestingly, Ni metal nanoparticles are in-situ exsolved on both Ni-SFM and Ni-GDC surfaces after reduction, resulting in Ni@Ni-SFM/Ni-GDC dual-exsolved self-assembled cathode. By combining the advantages of self assembly and in-situ exsolution, a SOEC using the Ni@Ni-SFM/Ni-GDC cathode exhibits a current density of  $1.72 \text{ A cm}^{-2}$  at  $800^\circ\text{C}$  and  $1.5 \text{ V}$ , remarkably higher than that of the Ni-SFM/Ni-GDC-based SOEC ( $0.89 \text{ A cm}^{-2}$  at  $800^\circ\text{C}$  and  $1.5 \text{ V}$ ). Moreover, the SOEC with the Ni@Ni-SFM/Ni-GDC cathode demonstrates outstanding CO selectivity and good durability. Theoretical calculations indicate that not only Ni@Ni-SFM but also Ni@Ni-GDC heterointerfaces are intrinsically active for  $\text{CO}_2\text{RR}$ , delivering lower energy barriers than that of the pristine SFM.

## 2. Experimental section

### 2.1. Materials preparation

Ni@Ni-Sr<sub>2</sub>Fe<sub>1.5</sub>Mo<sub>0.5</sub>O<sub>6-δ</sub>(SFM)/Ni-Gd<sub>0.1</sub>Ce<sub>0.9</sub>O<sub>2-δ</sub>(GDC) was synthesized using a facile one-pot self-assembled method. The mass ratio of Ni-SFM: Ni-GDC was 6:4, and the assumed molar ratio of Ni doping into SFM and GDC were 10% and 5%, respectively. Stoichiometric amounts of  $\text{Ni}(\text{NO}_3)_2 \bullet 6 \text{ H}_2\text{O}$ ,  $\text{Sr}(\text{NO}_3)_2$ ,  $\text{Fe}(\text{NO}_3)_3 \bullet 9 \text{ H}_2\text{O}$ ,  $(\text{NH}_4)_6\text{Mo}_7\text{O}_{24} \bullet 4 \text{ H}_2\text{O}$ ,  $\text{Gd}(\text{NO}_3)_3 \bullet 6 \text{ H}_2\text{O}$  and  $\text{Ce}(\text{NO}_3)_3 \bullet 6 \text{ H}_2\text{O}$  (all analytical purity, Sinopharm Chemical Reagent Co., Ltd.) starting materials were dissolved in deionized water. Complexing agents including citric acid monohydrate and glycolic acid were then introduced, resulting in a homogeneous solution. The as-prepared solution was continuously stirred at  $70^\circ\text{C}$  for 4 h until a viscous gel formed, followed via being dried at  $250^\circ\text{C}$  for 1 h to obtain a fluffy precursor. The precursor was sintered at  $1100^\circ\text{C}$  for 5 h in air to receive self-assembled Ni-doped SFM/GDC composite. The mass ratio of Ni-doped SFM and Ni-doped GDC was approximately 6:4. During cell operation, in-situ reduction in  $\text{H}_2$  at  $800^\circ\text{C}$  for 0.5 h caused the exsolution of Ni metal nanoparticles on the surfaces of both Ni-doped SFM and Ni-doped GDC, resulting in the desired dual-exsolved self-assembled Ni@Ni-SFM/Ni-GDC composite. In addition,  $\text{La}_{0.8}\text{Sr}_{0.2}\text{Ga}_{0.8}\text{Mg}_{0.2}\text{O}_{3-\delta}$  (LSGM) electrolyte and  $\text{PrBa}_{0.5}\text{Sr}_{0.5}\text{Co}_{1.5}\text{Fe}_{0.5}\text{O}_{5+\delta}$  (PBSCF)/GDC anode powders were synthesized via the same one-pot way.

### 2.2. Cell fabrication and testing

Electrolyte-supported electrolysis cells with a sandwich configuration of Ni@Ni-SFM/Ni-GDC cathode|LSGM electrolyte|PBSCF/GDC anode were manufactured. The LSGM electrolyte pellets were prepared via dry-pressing technology and were sintered at  $1400^\circ\text{C}$  for 5 h, resulting in a thickness of  $\sim 270 \mu\text{m}$ . The as-prepared anode and cathode powders were separately dispersed in terpineol solution at a mass ratio of 1:2 (powder:glue), to gain anode and cathode slurries. The resulting anode and cathode slurries were independently coated on the two sides of LSGM electrolyte disks and were subsequently calcined at  $1000^\circ\text{C}$  for 3 h to create the Ni@Ni-SFM/Ni-GDC|LSGM|PBSCF/GDC cells. Additionally, Ag paste was applied on both anode and cathode for current collection.

Electrochemical  $\text{CO}_2\text{RR}$  performances of single electrolysis cells were carried out using an electrochemical workstation (Ref3000, Gamry). Prior to the electrochemical tests, the cathode was in-situ reduced in  $\text{H}_2$  atmosphere at  $800^\circ\text{C}$  for 0.5 h to realize metal exsolution. During  $\text{CO}_2$  electrolysis, the Ni@Ni-SFM/Ni-GDC cathode was fed with pure  $\text{CO}_2$  at a flow rate of  $50 \text{ ml min}^{-1}$ , whereas the PBSCF/GDC anode was exposed to static air. The current-voltage (I-V) curves and electrochemical impedance spectroscopy (EIS) of the single cells were measured from  $800^\circ\text{C}$  to  $600^\circ\text{C}$ . The frequency range of impedance measurements was from 1 MHz to 0.01 Hz. The EIS curves were fitted based on the distribution of relaxation time (DRT) method [51,52]. The gas product was identified via a gas chromatograph (GC, Agilent 7890) to calculate faraday efficiency. In the case of stability test, the electrolysis cell was operated at an applied electrolytic voltage of 1.2 V.

### 2.3. Material characterization

Electrode and electrolyte powders were characterized by X-ray diffraction (XRD, Bruker D8-Focus) to identify phase structures. Scanning electron microscopy (SEM) images were obtained on a Hitachi SU-8010. High resolution transmission electron microscopy (HRTEM) and energy spectrometer (EDS) mapping were conducted on a Titan G260–300. Surface chemical states were determined by X-ray photoelectron spectroscopy (XPS, Kratos Axis Ultra DLD) with Al K $\alpha$  X-ray source. The standard C 1 s binding energy located at 284.8 eV was applied for calibration. Oxygen vacancies concentration was evaluated using electron paramagnetic resonance (EPR, Bruker-A300). Temperature-programmed desorption of  $\text{CO}_2$  ( $\text{CO}_2\text{-TPD}$ ) were recorded on a Micromeritics Chemisorption Analyzer (Auto Chem II 2920) to study the  $\text{CO}_2$  desorption over a temperature range of room temperature to  $900^\circ\text{C}$ .

### 2.4. Computational details

To conduct density functional theory (DFT) calculations, the first-principles were employed using the Vienna Ab-initio Simulation Packages (VASP). The generalized gradient approximation (GGA) with the Perdew-Burke-Ernzerhof (PBE) formulation was used to describe the exchange-correlation potential effect [53]. The projected augmented wave (PAW) [54,55] pseudopotentials were adopted to address ionic cores and take valence electrons into account, with a plane-wave kinetic energy cutoff to 520 eV. Partial occupancies of the Kohn–Sham orbitals were allowed using the Gaussian smearing approach with a width of 0.05 eV. To ensure convergence, the energies and residual forces were, respectively, converged to  $10^{-5} \text{ eV}$  and  $0.05 \text{ eV } \text{\AA}^{-1}$ . A vacuum layer of 20 Å was implemented to separate the periodic slabs. The Brillouin zone integration was performed using  $2 \times 2 \times 1$  Monkhorst-Pack k-point sampling for a structure. The cubic perovskite structure of SFM and the cubic fluorite structure of GDC were built for geometry optimization. Ni cluster was introduced onto Ni-SFM (001) and Ni-GDC (111) surfaces, respectively. Partial density of states of SFM, Ni@Ni-SFM, Ni@Ni-GDC were calculated. One surface oxygen was removed to simulate the

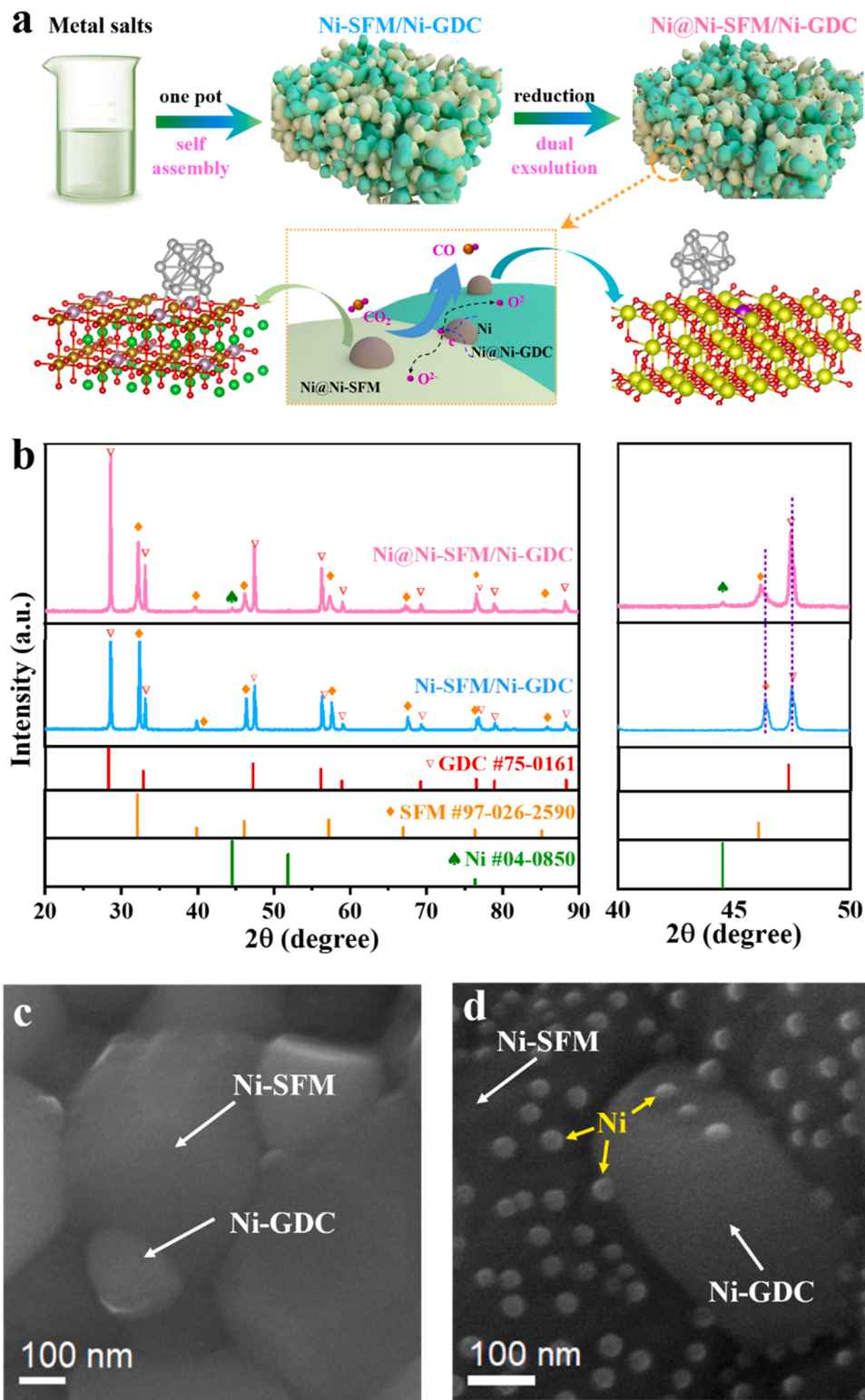


**Fig. 1.** (a) Synthesis scheme of Ni@Ni-SFM/Ni-GDC, (b) XRD patterns of Ni-SFM/Ni-GDC and Ni@Ni-SFM/Ni-GDC powders, SEM images of (c) Ni-SFM/Ni-GDC and (d) Ni@Ni-SFM/Ni-GDC powders.

oxygen vacancy in each model. The adsorption energies ( $E_{ads}$ ) were calculated, according to  $E_{ads} = E_{ad/sub} - E_{ad} - E_{sub}$ , where  $E_{ad/sub}$ ,  $E_{ad}$ , and  $E_{sub}$  represented the energies of the optimized adsorbate/substrate structure, the adsorbate in the structure, and the pristine substrate, respectively. Subsequently, the free energy was calculated by the equation:  $G = E_{ads} + ZPE \cdot TS$ , where the  $E_{ads}$ , ZPE, T, and S denoted the

calculated total energy, the zero-point energy, the temperature, and the entropy, respectively.

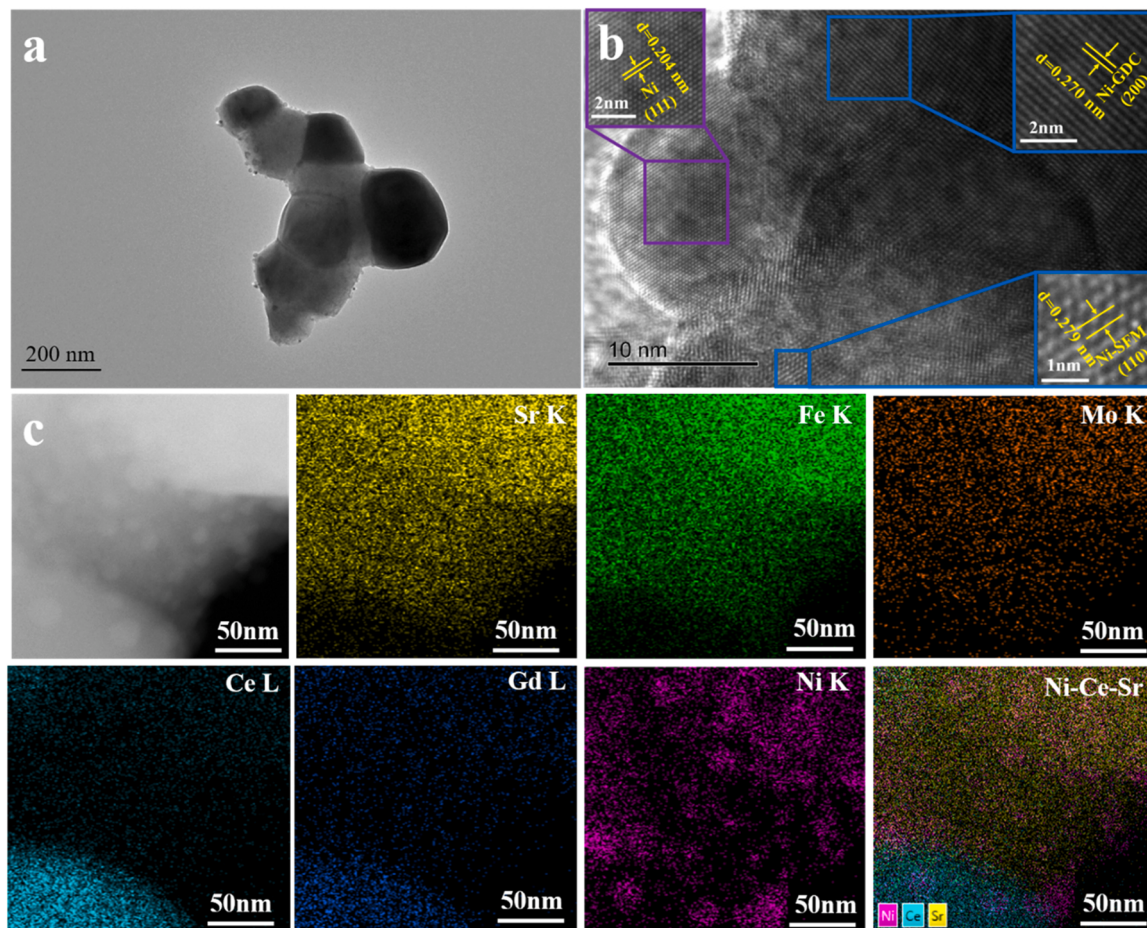


**Fig. 2.** (a) Low magnification, (b) High magnification HRTEM images, and (c) corresponding EDS element mapping of Ni@Ni-SFM/Ni-GDC powder.

### 3. Results and discussion

#### 3.1. Phase and structure

The synthetic route diagram of the dual-exsolved self-assembled Ni@Ni-SFM/Ni-GDC cathode is depicted in Fig. 1a. Initially, the stoichiometric metal salts were self-assembled using a one-pot sol-gel method to form the Ni-SFM/Ni-GDC composite precursor. Then, after in-situ reduction during electrolysis cell operation, Ni nanoparticles were dual-exsolved on both Ni-SFM and Ni-GDC surfaces, resulting in the dual-exsolved self-assembled Ni@Ni-SFM/Ni-GDC composite cathode. Phase structures of the as-prepared Ni-SFM/Ni-GDC and Ni@Ni-SFM/Ni-GDC powders before and after reduction were analyzed by X-ray diffraction (XRD). As shown in Fig. 1b, the self-assembly of a perovskite structure ( $\text{Sr}_2\text{Fe}_{1.5}\text{Mo}_{0.5}\text{O}_{6-\delta}$ , PDF #00–003–1109) [19] and a fluorite structure (GDC, PDF#75–0161)[56] are received in Ni-SFM/Ni-GDC composite cathode. No impurity phases are detected, suggesting that the Ni element is likely incorporated into the lattice. After reduction, an additional peak at  $44.1^\circ$  is recorded, which is well indexed to the metallic Ni (PDF #04–0850) [57]. This indicates that partial Ni is exsolved from Ni-SFM/Ni-GDC composite during reduction process. Moreover, the typical diffraction peaks of both Ni-SFM and Ni-GDC shift to lower angles, indicative of enhanced lattice parameters. These lattice expansions are likely attributed to the reduction of metal valence states with larger ionic radius. Additionally, the powders of LSGM electrolyte and PBSCF/GDC composite anode were also successfully prepared by the one-pot method (Fig. S1).

Fig. 1c and d provide the scanning electron microscopy (SEM) morphology of Ni-SFM/Ni-GDC and Ni@Ni-SFM/Ni-GDC powders. The

Ni-SFM/Ni-GDC composite appears to have a smooth and clean surface. After reduction, numerous spherical nanoparticles with an average size of approximately 20 nm are created on the surface and in the interface of Ni-SFM/Ni-GDC. For more detailed analysis on the microstructures, high resolution transmission electron microscopy (HRTEM) and energy spectrometer (EDS) mapping were performed. For Ni-SFM/Ni-GDC, lattice spacings of 0.278 nm and 0.270 nm are obtained (Fig. S2), corresponding to the (110) plane of Ni-SFM and the (200) plane of Ni-GDC as determined by XRD analysis. Of note, energy dispersive spectrometer (EDS) mapping analysis shows that the Ni element is incorporated in both Ni-SFM and Ni-GDC particles. In the case of Ni@Ni-SFM/Ni-GDC, tiny nanoparticles are observed to exsolve onto the surfaces of Ni-SFM and Ni-GDC substrates (Fig. 2a). In addition to Ni-SFM (110) and Ni-GDC (200) planes, a lattice spacing of the newly created nanoparticle is 0.204 nm, consistent with the (111) plane of metallic Ni (Fig. 2b). Moreover, the exsolved metallic Ni nanoparticle is firmly coupled with Ni-SFM and Ni-GDC substrates, indicating the strong metal-oxide interactions in both Ni@Ni-SFM and Ni@Ni-GDC heterointerfaces. These strong interactions have great potential to offer synergistic catalysis for  $\text{CO}_2\text{RR}$  and inhibit exsolved metal nanoparticles against agglomeration and carbon deposition.[38] As depicted in EDS mapping for Ni@Ni-SFM/Ni-GDC (Fig. 2c), the primary exsolved metal on the surfaces and in the interface of Ni-SFM and Ni-GDC might be Ni. As reported, the co-segregation energy of Ni is lower than that of Fe, and is thereby more readily exsolved than Fe [32]. These results denote that the successful preparation of a dual-exsolved self-assembled Ni@Ni-SFM/Ni-GDC cathode by a combined one-pot and in-situ exsolution way. Interestingly, the dual-exsolution and dual-dissolution of metal nanoparticles are almost reversible during reduction-oxidation

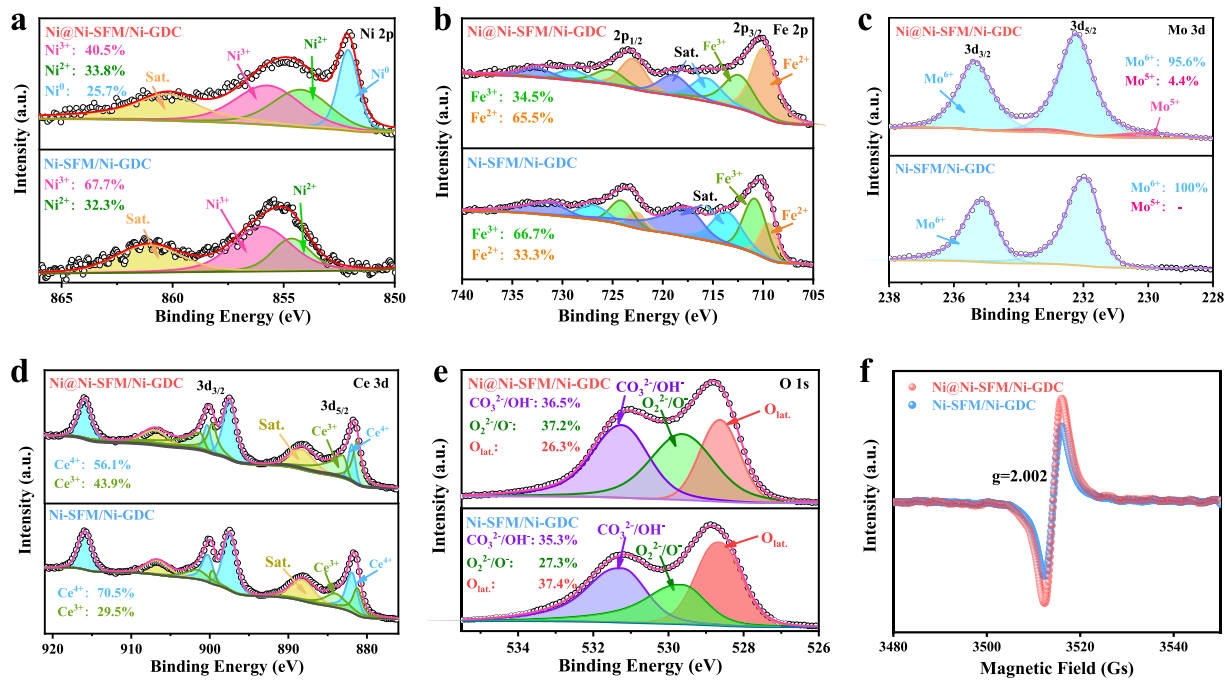


Fig. 3. XPS (a) Ni 2p, (b) Fe 2p, (c) Mo 3d, (d) Ce 3d, (e) O1s spectra, and (f) EPR spectra of Ni-SFM/Ni-GDC and Ni@Ni-SFM/Ni-GDC powders.

cycle, as evidenced by XRD (Fig. S3) and SEM (Fig. S4) analysis.

X-ray photoelectron spectroscopy (XPS) was employed to analyze the surface chemical variation between Ni-SFM/Ni-GDC and Ni@Ni-SFM/Ni-GDC cathodes. As described in Fig. 3a, besides Ni<sup>3+</sup> and Ni<sup>2+</sup>, Ni<sup>0</sup> is monitored on the surface of Ni@Ni-SFM/Ni-GDC,[58] denoting that metallic Ni is generated after reduction process. It is worth noting that

the average valence states of Ni (Fig. 3a), Fe (Fig. 3b), Mo (Fig. 3c) and Ce (Fig. 3d) are reduced in Ni-SFM/Ni-GDC compared to Ni@Ni-SFM/Ni-GDC. For example, the fitted molar ratio of Ce<sup>4+</sup>: Ce<sup>3+</sup> decreases from 70.5%: 29.5% in Ni-SFM/Ni-GDC to 56.1%: 43.9% in Ni@Ni-SFM/Ni-GDC. In order to meet the electroneutrality, the decreased valence states of cations are compensated by the creation of

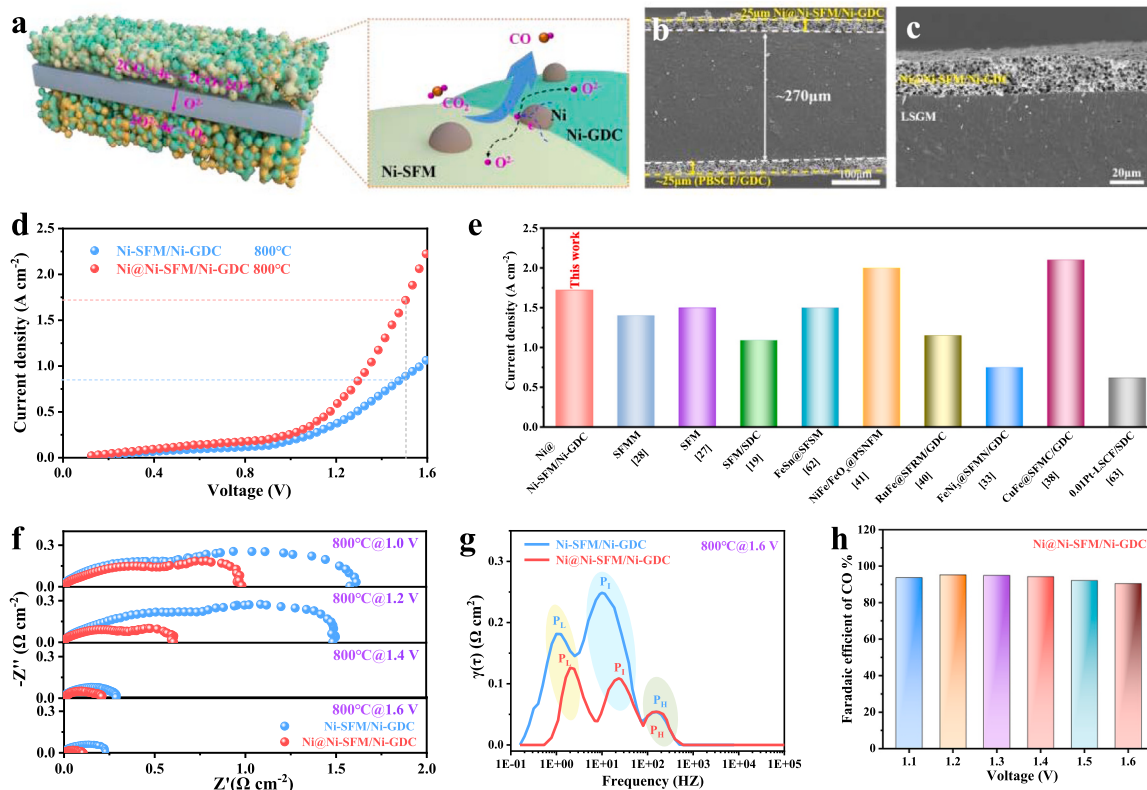
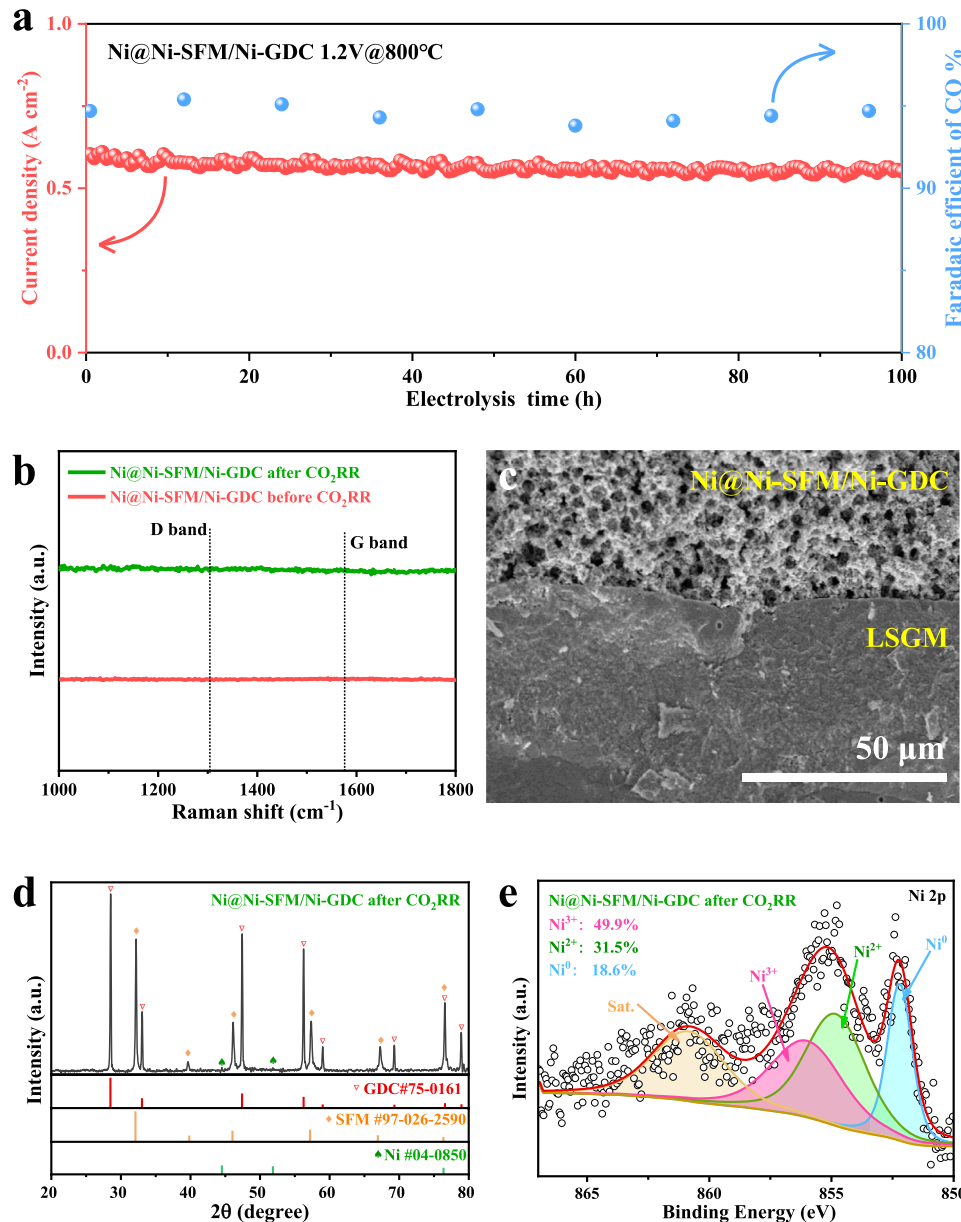


Fig. 4. (a) Schematic diagram of SOEC for CO<sub>2</sub> electrolysis, SEM images of (b) total SOEC and (c) Ni@Ni-SFM/Ni-GDC cathode, (d) I–V curves, (e) Comparison of electrochemical performance, (f) EIS plots, (g) DRT curves and (h) Faraday efficiency of CO production of the Ni@Ni-SFM/Ni-GDC based SOEC.



**Fig. 5.** (a) Constant voltage  $\text{CO}_2$  electrolysis curve and CO selectivity of the Ni@Ni-SFM/Ni-GDC based SOEC at 1.2 V and 800 °C, (b) Raman spectrum of the Ni@Ni-SFM/Ni-GDC cathode before and after  $\text{CO}_2$  electrolysis, (c) SEM image, (d) XRD pattern, and (e) XPS Ni 2p spectrum of the Ni@Ni-SFM/Ni-GDC cathode after  $\text{CO}_2$  electrolysis.

oxygen vacancies. As depicted in Fig. 3e, the O 1 s XPS spectra are deconvoluted into lattice oxygen ( $\text{O}_{\text{lat}}$ ) at 528.6 eV, highly oxidative oxygen ( $\text{O}_2^{\cdot}/\text{O}$ ) at 529.7 eV, and carbonate/hydroxyl oxygen species ( $\text{CO}_3^{2-}/\text{OH}^-$ ) at 531.3 eV [33]. It is clear that the highly oxidative oxygen species are enhanced from Ni-SFM/Ni-GDC to Ni@Ni-SFM/Ni-GDC, suggestive of increased oxygen vacancies on the surface of the Ni@Ni-SFM/Ni-GDC. In electron paramagnetic resonance (EPR) spectra (Fig. 3f), the Ni@Ni-SFM/Ni-GDC shows more spin numbers of the lone electrons than that of the Ni-SFM/Ni-GDC, further denoting a higher concentration of oxygen vacancies in the Ni@Ni-SFM/Ni-GDC [59–61]. Of note, the presence of oxygen vacancies not only facilitates surface  $\text{CO}_2$  adsorption but also accelerates bulk oxygen ionic conduction [28].

To investigate the  $\text{CO}_2$  adsorption behavior on Ni-SFM/Ni-GDC and Ni@Ni-SFM/Ni-GDC,  $\text{CO}_2$  temperature programmed desorption ( $\text{CO}_2$ -TPD) was performed and the results are provided in Fig. S5. The  $\text{CO}_2$  desorption at low-temperature range (50–200 °C) corresponds to the physical desorption of monodentate carbonates and linearly adsorbed

$\text{CO}_2$ , whereas the  $\text{CO}_2$  desorption at elevated temperatures (400–800 °C) is attributed to the chemical desorption. It is evident that the chemical adsorption capacity of Ni@Ni-SFM/Ni-GDC is higher than that of Ni-SFM/Ni-GDC. This may originate from the newly created adsorption sites in the interfaces of metal-oxide heterostructures and the surfaces of oxygen vacancies enriched oxides induced by dual-exsolution, thereby benefiting the prerequisite for  $\text{CO}_2$ RR.

### 3.2. Electrochemical performances

Fig. 4a illustrates the schematic diagram of the SOEC electrolysis cell featuring a sandwich construction of Ni@Ni-SFM/Ni-GDC (cathode) | LSGM (electrolyte) | PBSCF/GDC (anode). The thickness of the LSGM electrolyte supporting layer is about 270  $\mu\text{m}$ , while the Ni@Ni-SFM/Ni-GDC cathode and PBSCF/GDC anode are approximately 25  $\mu\text{m}$  thick (Fig. 4b). A well contacted interface between cathode and electrolyte is observed (Fig. 4c), ensuring high interfacial stability and rapid

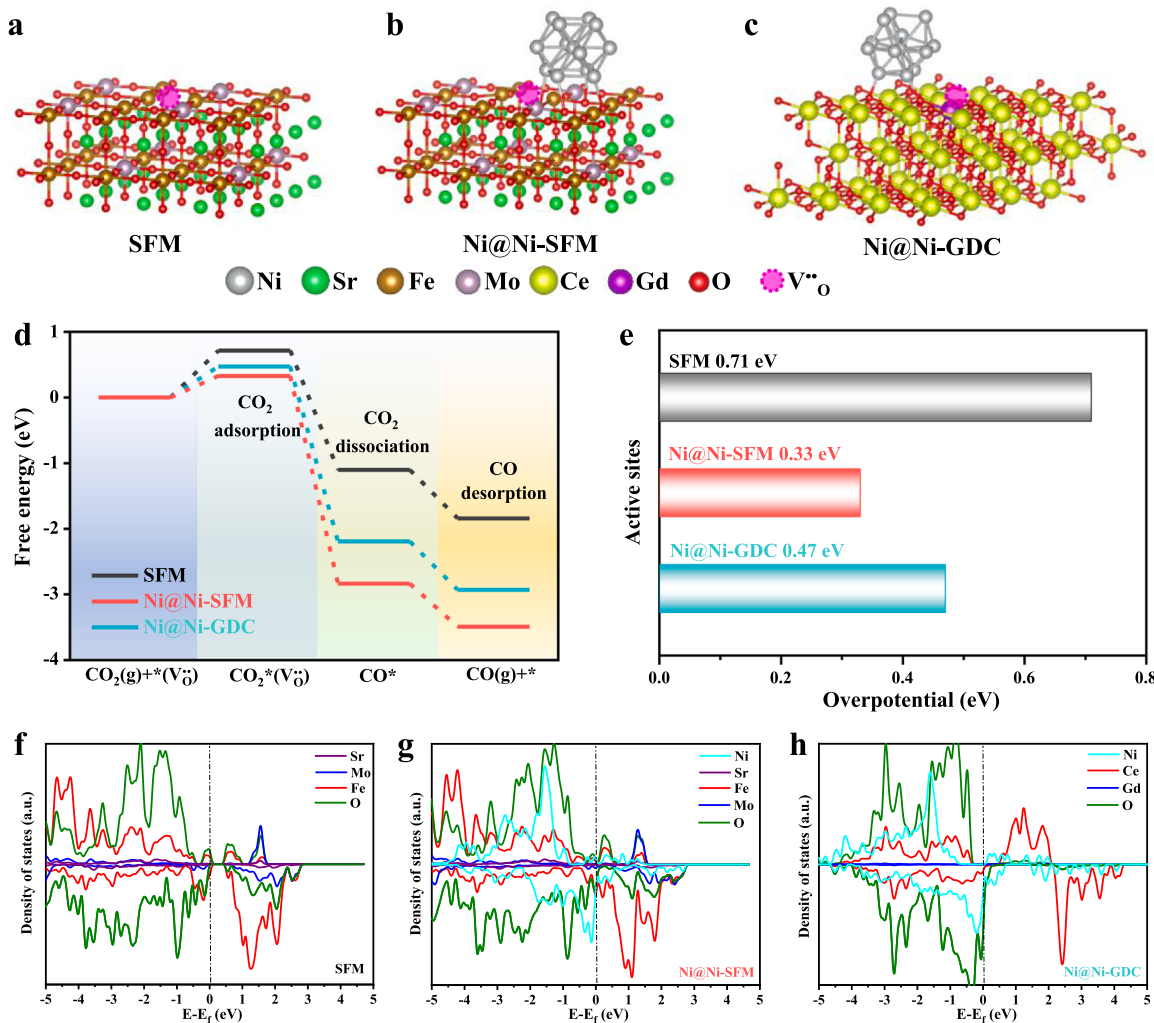


**Fig. 6.** Constructed oxygen defective (a) SFM, (b) Ni@Ni-SFM, (c) Ni@Ni-GDC surfaces for CO<sub>2</sub>RR, (d) Free-energy diagrams, (e) Theoretical overpotentials of SFM, Ni@Ni-SFM, Ni@Ni-GDC, Density of states of (f) SFM, (g) Ni@Ni-SFM, and (h) Ni@Ni-GDC.

interfacial ionic transfer. Figs. S6 and S7 present the typical current–voltage (I–V) curves of SOEC with the Ni-SFM/Ni-GDC cathode and the Ni@Ni-SFM/Ni-GDC cathode for CO<sub>2</sub> electrocatalysis from 800 °C to 600 °C. One can see that the current densities are enhanced after in-situ exsolution. For instance, the current density of the SOEC using the Ni@Ni-SFM/Ni-GDC cathode is 1.72 A cm<sup>-2</sup> at 800 °C and 1.5 V (Fig. 4d), superior to the Ni-SFM/Ni-GDC cathode (0.89 A cm<sup>-2</sup>) and most state-of-the-art cathodes (Fig. 4e and Table S1) [19,27,28,33,38, 40,41,62,63].

As shown in Fig. 4f, the electrode polarization resistances ( $R_p$ ) under various applied potentials are significantly reduced after in-situ reduction, indicating that the reaction kinetics of CO<sub>2</sub>RR is accelerated by dual-exsolution. Distribution of relaxation time (DRT) method was implemented to decouple the multiple electrochemical processes. As depicted in Fig. 4g, the polarization curves are divided into high frequency polarization ( $P_H$ ), intermediate frequency polarization ( $P_I$ ), and low frequency polarization ( $P_L$ ), which correspond to the oxygen evolution reaction in the anode and the O<sup>2-</sup> transfer in the electrolyte/electrode interface, the CO<sub>2</sub>RR and O<sup>2-</sup> diffusion in the cathode, and CO<sub>2</sub> adsorption, respectively [33,37]. Due to almost the same anodes and electrolytes, the SOEC using Ni@Ni-SFM/Ni-GDC cathode and Ni-SFM/Ni-GDC cathode possess similar high frequency resistances. It is noteworthy that the intermediate frequency and low frequency resistances are substantially reduced after in-situ reduction, implying the enhanced CO<sub>2</sub>RR dynamics and promoted CO<sub>2</sub> adsorption induced by

dual-exsolution. Moreover, Fig. 4h illustrates the CO faradaic efficiency of the SOEC with the Ni@Ni-SFM/Ni-GDC cathode. With the applied electrolysis voltage ranging from 1.1 V to 1.6 V, the CO faradaic efficiency increases firstly and then decreases. The highest CO faradaic efficiency of 95.2% is achieved at 1.2 V, suggestive of excellent product selectivity of CO. As revealed, the perovskite-based electrodes usually exhibit high tolerance against carbon deposition, thus demonstrating high CO selectivity [12].

The durability assessment of the Ni@Ni-SFM/Ni-GDC based SOEC for CO<sub>2</sub>RR was evaluated at 800 °C with an electrolysis voltage of 1.2 V. The current density as well as CO selectivity remain almost stable without obvious degradation for 100 h continuous electrolysis (Fig. 5a). Raman measurements were carried out on the Ni@Ni-SFM/Ni-GDC surface before and after continuous CO<sub>2</sub> electrolysis. The absence of typical C-C peaks at 1338 and 1568 cm<sup>-1</sup> suggests almost no carbon deposition (Fig. 5b). Considering that the possible reduction products of CO<sub>2</sub> electrolysis by SOEC are CO and C, such high tolerance against carbon deposition signifies high selectivity of CO. Meanwhile, the architectures of cathode and cathode-electrolyte interface remain stable after long-term CO<sub>2</sub>RR operation (Fig. 5c). XRD (Fig. 5d) together with XPS (Fig. 5e) results further indicate the good stability of the Ni@Ni-SFM/Ni-GDC cathode. In addition, the reoxidation of Ni@Ni-SFM/Ni-GDC after long-term CO<sub>2</sub> electrolysis was further performed. Interestingly, the cathode turns into Ni-SFM/Ni-GDC again (Fig. S8), indicating that the reversibility of exsolution/dissolution is still achieved after

long-term CO<sub>2</sub> electrolysis. These electrochemical assessments of SOEC reveal that the dual-exsolved self-assembled Ni@Ni-SFM/Ni-GDC is a highly active and stable cathode of SOEC for CO<sub>2</sub>RR.

### 3.3. Electrocatalytic CO<sub>2</sub> reduction mechanism

We conducted density functional theory (DFT) calculations to understand the possible CO<sub>2</sub>RR pathway on Ni@Ni-SFM, Ni@Ni-GDC heterointerfaces, as well as the pristine SFM for comparison. As known, the realistic surface and heterointerface models are more complicated because of the diverse crystal planes and non-stoichiometric defects. Here, we only consider the ideal modes of Ni cluster@Ni-SFM (001), Ni cluster@Ni-GDC (111), and pristine SFM (001). An oxygen vacancy is, respectively, built on each SFM (Fig. 6a), Ni@Ni-SFM (Fig. 6b) and Ni@Ni-GDC (Fig. 6c) surfaces to accommodate the product of lattice oxygen. A widely accepted SOEC mechanism for CO<sub>2</sub>RR involves three elementary processes of CO<sub>2</sub> adsorption, CO<sub>2</sub> dissociation, and CO desorption [40]. The adsorption structures of reaction intermediates on SFM, Ni@Ni-SFM and Ni@Ni-GDC are illustrated in Figs. S9, S10, and S11, and the corresponding Gibbs free energy diagram are provided in Fig. 6d. It is inferred that the rate-determining step for SFM, Ni@Ni-SFM and Ni@Ni-GDC is CO<sub>2</sub> adsorption. The CO<sub>2</sub> adsorption energy of SFM, Ni@Ni-SFM and Ni@Ni-GDC are 0.71 eV, 0.33 eV, and 0.47 eV, respectively (Fig. 6e). Consequently, the Ni@Ni-SFM and Ni@Ni-GDC heterointerfaces with the lower overpotentials represent higher intrinsic activities for CO<sub>2</sub>RR than the pristine SFM.

Furthermore, the calculated partial densities of states (DOS) of SFM, Ni@Ni-SFM and Ni@Ni-GDC are shown in Fig. 6f, g, and h. The DOS of exsolved Ni@Ni-SFM and Ni@Ni-GDC heterointerfaces around Fermi level are much richer than that of SFM, contributing to CO<sub>2</sub> adsorption and activation [64]. Meanwhile, the exsolved Ni@Ni-SFM and Ni@Ni-GDC heterointerfaces with no band gaps promise enhanced electronic transmission for CO<sub>2</sub>RR electrocatalysis compared to SFM. Additionally, the heterointerface between Ni-SFM and Ni-GDC might also contribute to CO<sub>2</sub>RR electrocatalysis, since the cooperation of doped cerium oxide can increase the number of active sites and facilitate oxygen ionic transfer [19,44].

## 4. Conclusions

In summary, a novel dual-exsolved self-assembled cathode of SOEC is developed for CO<sub>2</sub>RR. By utilizing in-situ dual-exsolution strategy, metallic Ni nanoparticles are exsolved on self-assembled Ni doped Sr<sub>2</sub>Fe<sub>1.5</sub>Mo<sub>0.5</sub>O<sub>6-δ</sub> (Ni-SFM) and Ni doped Gd<sub>0.1</sub>Ce<sub>0.9</sub>O<sub>2-δ</sub> (Ni-GDC) composite surfaces. The resulting Ni@Ni-SFM/Ni-GDC cathode based SOEC demonstrates high activity and good durability for CO<sub>2</sub>RR. Notably, a high current density of 1.72 A cm<sup>-2</sup> at 800 °C and 1.5 V is received over the SOEC using Ni@Ni-SFM/Ni-GDC cathode, favorably outperforming most reported cathode materials for SOEC. As unveiled by theoretical calculation, the Ni@Ni-SFM and Ni@Ni-GDC heterointerfaces facilitate CO<sub>2</sub> adsorption, contributing to promoted intrinsic activities for CO<sub>2</sub>RR. This study sheds light on the rational design of dual-exsolved cathode materials of SOEC for CO<sub>2</sub>RR electrolysis.

## CRediT authorship contribution statement

**Feng Hu:** Data curation, Formal analysis, Conceptualization, Methodology, Investigation. **Yihan Ling:** Investigation. **Siyu Fang:** Data curation, **Longtao Sui, Huangwei Xiao:** Formal analysis. **Yonglong Huang:** Data curation. **Sijiao Wang:** Software. **Beibei He:** Funding acquisition, Supervision, Writing – review & editing. **Ling Zhao:** Writing – original draft, Formal analysis, Funding acquisition, Supervision, Writing – review & editing.

## Declaration of Competing Interest

The authors declare that they have no known competing financial interests or personal relationships that could have appeared to influence the work reported in this paper.

## Data availability

Data will be made available on request.

## Acknowledgements

We gratefully acknowledge the financial support from the National Natural Science Foundation of China (No. 22075256 & No. 21975229), Natural Science Foundation of Zhejiang Province (No. LY23E020004 & No. LY23B030004), and Shenzhen Science and Technology Program (No. JCYJ20220530162403008).

## Appendix A. Supporting information

Supplementary data associated with this article can be found in the online version at doi:10.1016/j.apcatb.2023.122968.

## References

- [1] Y. Zheng, Z.W. Chen, J.J. Zhang, Solid oxide electrolysis of H<sub>2</sub>O and CO<sub>2</sub> to produce hydrogen and low-carbon fuels, *Electrochim. Energy Rev.* 4 (2021) 508–517.
- [2] W.P. Li, J.L. Luo, High-temperature electrochemical devices based on dense ceramic membranes for CO<sub>2</sub> conversion and utilization, *Electrochim. Energy Rev.* 4 (2021) 518–544.
- [3] Y.P. Zang, P.F. Wei, H.F. Li, D.F. Gao, G.X. Wang, Catalyst design for electrolytic CO<sub>2</sub> reduction toward low-carbon fuels and chemicals, *Electrochim. Energy Rev.* 5 (2022) 29.
- [4] X.D. Wang, Q. Hu, G.D. Li, H. Yang, C.X. He, Recent advances and perspectives of electrochemical CO<sub>2</sub> reduction toward C<sub>2+</sub> products on Cu-based catalysts, *Electrochim. Energy Rev.* 5 (2022) 28.
- [5] Y.Q. Chen, J.R. Zhang, L.J. Yang, X.Z. Wang, Q. Wu, Z. Hu, Recent advances in non-precious metal–nitrogen–carbon single-site catalysts for CO<sub>2</sub> electroreduction reaction to CO, *Electrochim. Energy Rev.* 5 (2022) 11.
- [6] X.Y. Wang, Y.H. Zou, Y.X. Zhang, B. Marchetti, Y.Y. Liu, J. Yi, X.D. Zhou, J. Zhang, Tin-based metal organic framework catalysts for high-efficiency electrocatalytic CO<sub>2</sub> conversion into formate, *J. Colloid Interf. Sci.* 626 (2022) 836–847.
- [7] G. Marcandalli, M.C.O. Monteiro, A. Goyal, M.T.M. Koper, Electrolyte effects on CO<sub>2</sub> electrochemical reduction to CO, *Acc. Chem. Res.* 55 (2022) 1900–1911.
- [8] L.T. Ye, Z.B. Shang, K. Xie, Selective oxidative coupling of methane to ethylene in a solid oxide electrolyser based on porous single-crystalline CeO<sub>2</sub> monoliths, *Angew. Chem. Int. Ed.* 61 (2022), e202207211.
- [9] M. Yin, Z.L. Wang, C.C. Yang, J. Pu, B. Chi, Improvement CO<sub>2</sub> electrocatalytic activity of LCTN fuel electrode for solid oxide electrolysis cells via an electro-reduction activation strategy, *J. Electrochim. Soc.* 170 (2023), 034501.
- [10] C.C. Yang, Y.F. Tian, J. Pu, B. Chi, Anion fluorine-doped La<sub>0.6</sub>Sr<sub>0.4</sub>Fe<sub>0.8</sub>Ni<sub>0.2</sub>O<sub>3-δ</sub> perovskite cathodes with enhanced electrocatalytic activity for solid oxide electrolysis cell direct CO<sub>2</sub> electrolysis, *ACS Sustain. Chem. Eng.* 10 (2022) 1047–1058.
- [11] E. Tezel, A. Whitten, G. Yarema, R. Denecke, J.S. McEwen, E. Nikolla, Electrochemical reduction of CO<sub>2</sub> using solid oxide electrolysis cells: insights into catalysis by nonstoichiometric mixed metal oxides, *ACS Catal.* 12 (2022) 11456–11471.
- [12] Y.A. Jiang, F.L. Chen, C.R. Xia, A review on cathode processes and materials for electro-reduction of carbon dioxide in solid oxide electrolysis cells, *J. Power Sources* 493 (2021), 229713.
- [13] Y. Zheng, J.C. Wang, B. Yu, W.Q. Zhang, J. Chen, J.L. Qiao, J.J. Zhang, A review of high temperature co-electrolysis of H<sub>2</sub>O and CO<sub>2</sub> to produce sustainable fuels using solid oxide electrolysis cells (SOECs): advanced materials and technology, *Chem. Soc. Rev.* 46 (2017) 1427–1463.
- [14] Y. Li, L. Zeng, G. Pang, X. Wei, M. Wang, K. Cheng, J. Kang, J.M. Serra, Q. Zhang, Y. Wang, Direct conversion of carbon dioxide into liquid fuels and chemicals by coupling green hydrogen at high temperature, *Appl. Catal. B: Environ.* 324 (2023), 122299.
- [15] A.D.N. Kamkeng, M.H. Wang, Long-term performance prediction of solid oxide electrolysis cell (SOEC) for CO<sub>2</sub>/H<sub>2</sub>O co-electrolysis considering structural degradation through modelling and simulation, *Chem. Eng. J.* 429 (2022), 132158.
- [16] H. Wang, F.K. Jiang, X. Wang, L.T. Ye, K. Xie, Enhanced CO<sub>2</sub> electrolysis with the modification of Ni-YSZ cathodes by SDC in microtubular solid oxide electrolysis cells, *Energy Fuel* 36 (2022) 13195–13202.

- [17] A.Q. Wu, B.B. Han, L.Z. Zhu, W.B. Guan, S.C. Singhal, Performance of CO<sub>2</sub> electrolysis using solid oxide electrolysis cell with Ni-YSZ as fuel electrode under different fuel atmospheres, *Int. J. Green. Energy* 19 (2022) 1209–1220.
- [18] V. Duboviks, R.C. Maher, M. Kishimoto, L.F. Cohen, N.P. Brandon, G.J. Offer, A. Raman spectroscopic study of the carbon deposition mechanism on Ni/CGO electrodes during CO/CO<sub>2</sub> electrolysis, *Phys. Chem. Chem. Phys* 16 (2014) 13063–13068.
- [19] Y.H. Li, X.R. Chen, Y. Yang, Y.N. Jiang, C.R. Xia, Mixed-conductor Sr<sub>2</sub>Fe<sub>1.5</sub>Mo<sub>0.5</sub>O<sub>6-δ</sub> as robust fuel electrode for pure CO<sub>2</sub> reduction in solid oxide electrolysis cell, *ACS Sustain. Chem. Eng.* 5 (2017) 11403–11412.
- [20] Y. Wang, T. Liu, S.M. Fang, F.L. Chen, Syngas production on a symmetrical solid oxide H<sub>2</sub>O/CO<sub>2</sub> coelectrolysis cell with Sr<sub>2</sub>Fe<sub>1.5</sub>Mo<sub>0.5</sub>O<sub>6-δ</sub>-Sm<sub>0.2</sub>Ce<sub>0.8</sub>O<sub>1.9</sub> electrodes, *J. Power Sources* 305 (2016) 240–248.
- [21] X.Y. Gao, L.T. Ye, K. Xie, Voltage-driven reduction method to optimize in-situ exsolution of Fe nanoparticles at Sr<sub>2</sub>Fe<sub>1.5+x</sub>Mo<sub>0.5</sub>O<sub>6-δ</sub> interface, *J. Power Sources* 561 (2023), 232740.
- [22] F. Bidrawn, G. Kim, G. Corre, J.T.S. Irvine, J.M. Vohs, R.J. Gorte, Efficient reduction of CO<sub>2</sub> in a solid oxide electrolyzer, *Electrochim. Solid-State Lett.* 11 (2008) B167–B170.
- [23] Y. Yang, Y.H. Li, Y.A. Jiang, M.H. Zheng, T. Hong, X.J. Wu, C.R. Xia, The electrochemical performance and CO<sub>2</sub> reduction mechanism on strontium doped lanthanum ferrite fuel electrode in solid oxide electrolysis cell, *Electrochim. Acta* 284 (2018) 159–167.
- [24] D.J. Deka, J. Kim, S. Gunduz, D. Jain, Y.J. Shi, J.T. Miller, A.C. Co, U.S. Ozkan, Coke formation during high-temperature CO<sub>2</sub> electrolysis over AFeO<sub>3</sub> (A = La/Sr) cathode: Effect of A-site metal segregation, *Appl. Catal. B: Environ.* 283 (2021), 119642.
- [25] W.T. Qi, Y. Gan, D. Yin, Z.Y. Li, G.J. Wu, K. Xie, Y.C. Wu, Remarkable chemical adsorption of manganese-doped titanate for direct carbon dioxide electrolysis, *J. Mater. Chem. A* 2 (2014) 6904–6915.
- [26] Y.H. Li, Y. Li, Y.H. Wan, Y. Xie, J.F. Zhu, H.B. Pan, X.S. Zheng, C.R. Xia, Perovskite oxyfluoride electrode enabling direct electrolyzing carbon dioxide with excellent electrochemical performances, *Adv. Energy Mater.* 9 (2019) 1803156.
- [27] X.A. Xi, J.W. Liu, W.Z. Luo, Y. Fan, J.J. Zhang, J.L. Luo, X.Z. Fu, Unraveling the enhanced kinetics of Sr<sub>2</sub>Fe<sub>1+x</sub>Mo<sub>1-x</sub>O<sub>6-δ</sub> electrocatalysts for high-performance solid oxide cells, *Adv. Energy Mater.* 11 (2021) 2102845.
- [28] X.A. Xi, J.W. Liu, Y. Fan, L.J. Wang, J. Li, M.M. Li, J.L. Luo, X.Z. Fu, Reducing d-p band coupling to enhance CO<sub>2</sub> electrocatalytic activity by Mg-doping in Sr<sub>2</sub>FeMoO<sub>6-δ</sub> double perovskite for high performance solid oxide electrolysis cells, *Nano Energy* 82 (2021), 105707.
- [29] L.H. Zhang, C.M. Xu, W. Sun, R.Z. Ren, X.X. Yang, Y.Z. Luo, J.S. Qiao, Z.H. Wang, S.Y. Chen, K.N. Sun, Constructing perovskite/alkaline-earth metal composite heterostructure by infiltration to revitalize CO<sub>2</sub> electrolysis, *Sep. Purif. Technol.* 298 (2022), 121475.
- [30] T. Liu, H. Liu, X.Y. Zhang, L.B. Lei, Y.X. Zhang, Z.H. Yuan, F.L. Chen, Y. Wang, A robust solid oxide electrolyzer for highly efficient electrochemical reforming of methane and steam, *J. Mater. Chem. A* 7 (2019) 13550–13558.
- [31] Y.J. Zhou, T.F. Liu, Y.F. Song, H.F. Lv, Q.X. Liu, N. Ta, X.M. Zhang, G.X. Wang, Highly dispersed nickel species on iron-based perovskite for CO<sub>2</sub> electrolysis in solid oxide electrolysis cell, *Chinese. J. Catal.* 43 (2022) 1710–1718.
- [32] O. Kwon, S. Sengodan, K. Kim, G. Kim, H.Y. Jeong, J. Shin, Y.W. Ju, J.W. Han, G. Kim, Exsolution trends and co-segregation aspects of self-grown catalyst nanoparticles in perovskites, *Nat. Commun.* 8 (2017) 15967.
- [33] H.F. Lv, L. Lin, X.M. Zhang, D.F. Gao, Y.F. Song, Y.J. Zhou, Q.X. Liu, G.X. Wang, X. H. Bao, In situ exsolved FeNi<sub>3</sub> nanoparticles on nickel doped Sr<sub>2</sub>Fe<sub>1.5</sub>Mo<sub>0.5</sub>O<sub>6-δ</sub> perovskite for efficient electrochemical CO<sub>2</sub> reduction reaction, *J. Mater. Chem. A* 7 (2019) 11967–11975.
- [34] D.J. Deka, S. Gunduz, T. Fitzgerald, J.T. Miller, A.C. Co, U.S. Ozkan, Production of syngas with controllable H<sub>2</sub>/CO ratio by high temperature co-electrolysis of CO<sub>2</sub> and H<sub>2</sub>O over Ni and Co- doped lanthanum strontium ferrite perovskite cathodes, *Appl. Catal. B: Environ.* 248 (2019) 487–503.
- [35] B.B. Niu, C.L. Lu, W.D. Yi, S.J. Liao, X.W. Zhong, X.Z. Zhao, B.M. Xu, In-situ growth of nanoparticles-decorated double perovskite electrode materials for symmetrical solid oxide cells, *Appl. Catal. B: Environ.* 270 (2020), 118842.
- [36] J.X. Zhu, W.Q. Zhang, Y.F. Li, W.X. Yue, G. Geng, B. Yu, Enhancing CO<sub>2</sub> catalytic activation and direct electroreduction on in-situ exsolved Fe/MnO<sub>x</sub> nanoparticles from (PrBa)<sub>2</sub>Mn<sub>2-y</sub>Fe<sub>y</sub>O<sub>3+δ</sub> layered perovskites for SOEC cathodes, *Appl. Catal. B: Environ.* 268 (2020), 118389.
- [37] M.J. Ma, X.X. Yang, C.M. Xu, R.Z. Ren, J.S. Qiao, W. Sun, Z.H. Wang, K.N. Sun, Constructing highly active alloy-perovskite interfaces for efficient electrochemical CO<sub>2</sub> reduction reaction, *Sep. Purif. Technol.* 296 (2022), 121411.
- [38] F. He, M.Y. Hou, F. Zhu, D.L. Liu, H. Zhang, F.F. Yu, Y.C. Zhou, Y. Ding, M.L. Liu, Y. Chen, Building efficient and durable hetero-interfaces on a perovskite-based electrode for electrochemical CO<sub>2</sub> reduction, *Adv. Energy Mater.* 12 (2022) 2202175.
- [39] H.F. Lv, L. Lin, X.M. Zhang, Y.F. Song, H. Matsumoto, C.B. Zeng, N. Ta, W. Liu, D. F. Gao, G.X. Wang, X.H. Bao, In situ investigation of reversible exsolution/ dissolution of CoFe alloy nanoparticles in a Co-doped Sr<sub>2</sub>Fe<sub>1.5</sub>Mo<sub>0.5</sub>O<sub>6-δ</sub> cathode for CO<sub>2</sub> electrolysis, *Adv. Mater.* 32 (2020) 1906193.
- [40] H.F. Lv, L. Lin, X.M. Zhang, R.T. Li, Y.F. Song, H. Matsumoto, N. Ta, C.B. Zeng, Q. Fu, G.X. Wang, X.H. Bao, Promoting exsolution of RuFe alloy nanoparticles on Sr<sub>2</sub>Fe<sub>1.4</sub>Ru<sub>0.1</sub>Mo<sub>0.5</sub>O<sub>6-δ</sub> via repeated redox manipulations for CO<sub>2</sub> electrolysis, *Nat. Commun.* 12 (2021) 5665.
- [41] T. Tan, Z.M. Wang, M.X. Qin, W.T. Zhong, J.H. Hu, C.H. Yang, M.L. Liu, In situ exsolution of core-shell structured NiFe/FeO<sub>x</sub> nanoparticles on Pr<sub>0.4</sub>Sr<sub>1.6</sub>(NiFe) 1.5Mo<sub>0.5</sub>O<sub>6-δ</sub> for CO<sub>2</sub> electrolysis, *Adv. Funct. Mater.* 32 (2022) 2202878.
- [42] L.J. Ye, K. Zhu, Y.A. Jiang, S.W. Zhang, R.R. Peng, C.R. Xia, Carbon dioxide reduction processes on a samarium doped ceria electrocatalyst with exsolved Fe, Part. I, *J. Mater. Chem. A* 11 (2023) 10646–10658.
- [43] X.M. Zhang, Y.F. Song, F. Guan, Y.J. Zhou, H.F. Lv, G.X. Wang, X.H. Bao, Enhancing electrocatalytic CO<sub>2</sub> reduction in solid oxide electrolysis cell with Ce<sub>0.9</sub>Mn<sub>0.1</sub>O<sub>2-δ</sub> nanoparticles-modified LSCM-GDC cathode, *J. Catal.* 359 (2018) 8–16.
- [44] H.F. Lv, Y.J. Zhou, X.M. Zhang, Y.F. Song, Q.X. Liu, G.X. Wang, X.H. Bao, Infiltration of Ce<sub>0.8</sub>Gd<sub>0.2</sub>O<sub>1.9</sub> nanoparticles on Sr<sub>2</sub>Fe<sub>1.5</sub>Mo<sub>0.5</sub>O<sub>6-δ</sub> cathode for CO<sub>2</sub> electroreduction in solid oxide electrolysis cell, *J. Energy Chem.* 35 (2019) 71–78.
- [45] Y.S. Song, Y.B. Chen, W. Wang, C. Zhou, Y.J. Zhong, G.M. Yang, W. Zhou, M.L. Liu, Z.P. Shao, Self-assembled triple-conducting nanocomposite as a superior protonic ceramic fuel cell cathode, *Joule* 3 (2019) 2842–2853.
- [46] Y. Yang, Y.J. Wu, H. Bao, W.C. Song, H. Ni, D. Tian, B. Lin, P.Z. Feng, Y.H. Ling, An efficient and prospective self-assembled hybrid electrocatalyst for symmetrical and reversible solid oxide cells, *Electrochim. Acta* 362 (2020), 137171.
- [47] F. He, S. Liu, T. Wu, M.T. Yang, W.H. Li, G.M. Yang, F. Zhu, H. Zhang, K. Pei, Y. Chen, W. Zhou, Z.P. Shao, Catalytic self-assembled air electrode for highly active and durable reversible protonic ceramic electrochemical cells, *Adv. Funct. Mater.* 32 (2022) 2206756.
- [48] M. Machado, F. Baitutti, L. Bernadet, A. Morata, M. Nunez, J.P. Ouweltjes, F. C. Fonseca, M. Torrell, A. Tarancón, Functional thin films as cathode/electrolyte interlayers: a strategy to enhance the performance and durability of solid oxide fuel cells, *J. Mater. Chem. A* 10 (2022) 17317–17325.
- [49] K. Develops-Bagarinha, T. Ishiyama, H. Kishimoto, H. Shimada, K. Yamaji, Nanoengineering of cathode layers for solid oxide fuel cells to achieve superior power densities, *Nat. Commun.* 12 (2021) 3979.
- [50] H. Tong, M. Fu, Y. Yang, F.L. Chen, Z.T. Tao, A novel self-assembled cobalt-free perovskite composite cathode with triple-conduction for intermediate proton-conducting solid oxide fuel cells, *Adv. Funct. Mater.* 32 (2022) 2209695.
- [51] Y. Xu, Y. Huang, L.Y. Guo, F. Hu, M.J. Xu, W. Zhou, H.Z. Yang, J. Sun, B.B. He, L. Zhao, Engineering anion defect in perovskite oxyfluoride cathodes enables proton involved oxygen reduction reaction for protonic ceramic fuel cells, *Sep. Purif. Technol.* 290 (2022) 120844.
- [52] Y. Xu, F. Hu, Y.M. Guo, J. Zhang, Y.L. Huang, W. Zhou, J. Sun, B.B. He, L. Zhao, Probing oxygen reduction and water uptake kinetics of BaCo<sub>0.4</sub>Fe<sub>0.4</sub>Zr<sub>0.1</sub>Y<sub>0.1-x</sub>Zn<sub>x</sub>O<sub>3-δ</sub> cathodes for protonic ceramic fuel cells, *Sep. Purif. Technol.* 297 (2022), 121482.
- [53] J.P. Perdew, K. Burke, M. Ernzerhof, Generalized gradient approximation made simple, *Phys. Rev. Lett.* 77 (1996) 3865–3868.
- [54] G. Kresse, D. Joubert, From ultrasoft pseudopotentials to the projector augmented-wave method, *Phys. Rev. B* 59 (1999) 1758–1775.
- [55] P.E. Blochl, Projector augmented-wave method, *Phys. Rev. B* 50 (1994) 17953–17979.
- [56] L.J. Jia, T.M. Hu, F.Y. Liang, M.K. Liu, Y. Zhang, H.Q. Jiang, Enhanced CO<sub>2</sub>-tolerance and hydrogen separation performance of Ba-based ceramic membrane modified by Ce<sub>0.9</sub>Gd<sub>0.1</sub>O<sub>2-δ</sub> surface layer, *Sep. Purif. Technol.* 303 (2022) 122246.
- [57] L.Y. Hu, X. Zeng, X.Q. Wei, H.J. Wang, Y. Wu, W.L. Gu, L. Shi, C.Z. Zhu, Interface engineering for enhancing electrocatalytic oxygen evolution of NiFe LDH/NiTe heterostructures, *Appl. Catal. B: Environ.* 273 (2020), 119014.
- [58] K.Y. Zhu, T. Wu, M.R. Li, R.F. Lu, X.F. Zhu, W.S. Yang, Perovskites decorated with oxygen vacancies and Fe-Ni alloy nanoparticles as high-efficiency electrocatalysts for the oxygen evolution reaction, *J. Mater. Chem. A* 5 (2017) 19836–19845.
- [59] L.Q. Gui, Z.B. Wang, K. Zhang, B.B. He, Y.Z. Liu, W. Zhou, J.M. Xu, Q. Wang, L. Zhao, Oxygen vacancies-rich Ce<sub>0.9</sub>Gd<sub>0.1</sub>O<sub>2-δ</sub> decorated Pr<sub>0.5</sub>Ba<sub>0.5</sub>Co<sub>0.3</sub>O<sub>3-δ</sub> bifunctional catalyst for efficient and long-lasting rechargeable Zn-air batteries, *Appl. Catal. B: Environ.* 266 (2020), 118656.
- [60] M.S. You, L.Q. Gui, X. Ma, Z.B. Wang, Y. Xu, J. Zhang, J. Sun, B.B. He, L. Zhao, Electronic tuning of SrIrO<sub>3</sub> perovskite nanosheets by sulfur incorporation to induce highly efficient and long-lasting oxygen evolution in acidic media, *Appl. Catal. B: Environ.* 298 (2021), 120562.
- [61] M.S. You, Y. Xu, B.B. He, J. Zhang, L.Q. Gui, J.M. Xu, W. Zhou, L. Zhao, Realizing robust and efficient acidic oxygen evolution by electronic modulation of OD/2D CeO<sub>2</sub> quantum dots decorated SrIrO<sub>3</sub> nanosheets, *Appl. Catal. B: Environ.* 315 (2022), 121579.
- [62] J.W. Lv, W. Sun, C.M. Xu, X.X. Yang, M.J. Ma, L.H. Zhang, S.X. Zhang, J.S. Qiao, S. Y. Chen, K.N. Sun, Enhancing the catalytic activity and CO<sub>2</sub> chemisorption ability of the perovskite cathode for solid oxide electrolysis cell through in situ Fe-Sn alloy nanoparticles, *Sep. Purif. Technol.* 294 (2022), 121127.
- [63] W.C. Feng, Y.F. Song, X.M. Zhang, H.F. Lv, Q.X. Liu, G.X. Wang, X.H. Bao, Platinum-decorated ceria enhances CO<sub>2</sub> electroreduction in solid oxide electrolysis cells, *Chemsuschem* 13 (2020) 6290–6295.
- [64] H.F. Lv, T.F. Liu, X.M. Zhang, Y.F. Song, H. Matsumoto, N. Ta, C.B. Zeng, G. X. Wang, X.H. Bao, Atomic-scale insight into exsolution of CoFe alloy nanoparticles in La<sub>0.4</sub>Sr<sub>0.6</sub>Co<sub>0.2</sub>Fe<sub>0.7</sub>Mo<sub>0.1</sub>O<sub>3-δ</sub> with Efficient CO<sub>2</sub> Electrolysis, *Angew. Chem. Int. Ed.* 59 (2020) 15968–15973.